Supplementary Information for

Unveiling the distinct effect mechanisms of H_2O: Aggravating and mitigating SO_2 poisoning of Fe_2O_3 and α-MnO_2 catalysts in low-temperature NH_3-SCR

Jianyi Zhang[a,b,c,d §], *Hongyu Zhao*[a,b,c,d §], *Xuan Jia*[a,b,c,d], *Jinxiu Wang*[a,b,d*], *Jinsheng Chen*[a,b,d]

[a] State Key Laboratory of Advanced Environmental Technology, Institute of Urban Environment, Chinese Academy of Sciences, Xiamen 361021, P.R. China

[b] Fujian Key Laboratory of Atmospheric Ozone Pollution Prevention, Institute of Urban Environment, Chinese Academy of Sciences, Xiamen 361021, P.R. China

[c] College of Resources and Environment, Fujian Agriculture and Forestry University, Fuzhou 350002, P.R. China.

[d] University of Chinese Academy of Sciences, Beijing 100049, P.R. China

Corresponding Author

* Jinxiu Wang, Tel./Fax: +86 592 6190548, Email: jxwang@iue.ac.cn

§ Jianyi Zhang and Hongyu Zhao contributed equally to this paper.

Contents

S1 Characterization details

The crystal structure of the catalysts was characterized by X-ray powder diffraction (XRD). Prior to the measurements, all samples were thoroughly ground. The XRD patterns were acquired using a X'pert Pro diffractometer (PANalytical B.V., Holland) equipped with a Cu Kα radiation (λ = 0.15406 nm), operating at 40 kV and 40 mA. The scanning range was set from 10° to 90° (2θ). Semi-quantitative analysis of sulfur content in the poisoned catalyst powder was performed by Axios Max X-ray fluorescence spectrometer (XRF, PANalytical B.V., Holland). The concentrations of SO_4^{2-} and NH_4^+ ions in the solution of the poisoned catalyst were analyzed by ion chromatography (IC, 883 Basic IC plus, Metrohm AG, Switzerland), and the concentrations of soluble metals ions (Mn and Fe) were determined using inductively coupled plasma optical emission spectrometry (ICP-OES, Avio 220 Max, PerkinElmer, Inc., USA). The catalyst sample was processed as follows: 20 mg of the powdered sample was immersed in 5 mL of aqueous solution containing CH_2O (Guaranteed reagent, Sinopharm Chemical Reagent Co., Ltd., China) with 1% volume fraction and shaken continuously for 30 min. After soaking, the mixture was filtered through a 0.22 μm membrane, and 2 mL of the filtrate was taken for subsequent analysis. The CH_2O was added to the soaking solution of poisoned samples to inhibit the oxidation of sulfite during the testing procedure. Thermogravimetric analysis (TGA) coupled with derivative thermogravimetry (DTG) was performed on a Netzsch TG 209 F3 thermogravimetric analyzer (TG, Netzsch, Germany) to characterize the deposition of sulfur-containing species on the poisoned catalyst. The measurement was performed as follows: 10 mg of the catalyst powder was placed in a γ-Al_2O_3 crucible and heated to 950 °C under a N_2 atmosphere (60 mL/min) at a rate of 10 °C/min. The N_2 adsorption-desorption isotherms were obtained using a NOVA 2000e physisorption analyzer (Quantachrome Corp, USA). The specific surface area was calculated by the Brunauer–Emmett–Teller (BET) method, and the pore size distribution was derived from the adsorption branch of the isotherm using the Barrett–Joyner–Halenda (BJH) model. The measurement procedure was conducted as follows: 0.15 g of powdered sample was vacuum-pretreated

at 80 °C for 5 h to remove adsorbed impurities on the surface and within the pores. Subsequently, the N_2 adsorption-desorption experiment was performed at 77 k. X-ray photoelectron spectroscopy (XPS) measurements were carried out on an AXIS Supra instrument (Shimadzu, Japan) using a monochromatic Al Kα X-ray operated at 1486.8 eV and 150 W. All collected spectra were energy-referenced to the C 1s peak at 284.8 eV for calibration. H_2-temperature programmed reduction (H_2-TPR), temperature programmed desorption of NH_3 (NH_3-TPD), and O_2-temperature programmed desorption (O_2-TPD) analyses were conducted on a ChemBET-3000 TPR-TPD chemisorption apparatus (Quantachrome Instruments, USA) coupled with a DYCOR LC-D200 mass spectrometer (AMETEK Inc., USA). In the H_2-TPR experiment, 20 mg catalyst was placed in a U-shaped quartz reactor and pretreated under a He atmosphere at 100 ℃ for 60 min. After cooling to 35 ℃ approximately, the gas was switched to 5% H_2/Ar. The temperature was then ramped to 800 ℃ at a rate of 10 °C/min. For the NH_3-TPD test, 100 mg of catalyst powder was first purged under He flow at 180 °C for 90 min to remove impurities. After cooling to ~35 °C, the sample was exposed to 5 vol% NH_3/He for 40 min. Then, the He flow was introduced while ramping to 100 °C, where it was maintained for 45 min to remove physisorption NH_3. Finally, the temperature was increased to 700 °C at a rate of 10 °C/min under He flow. For O_2-TPD test, 50 mg catalyst powder was initially purged with He at 100 ℃ for 30 min and then was exposed to a 5% O_2/He (or 10% O_2/He) steam for 60 min after cooled down to 35 °C. Finally, the system was flushed with pure He, followed by temperature ramping to 800 ℃ at a rate of 10 °C/min. NO_x-temperature-programmed desorption (NO_x-TPD) was used to evaluate the NO_x adsorption capacity of the catalyst. NO_x-TPD tests were measured in a simulated fixed bed reactor with a quartz tube Φ 6.0 mm × 470 mm. First, 150 mg fresh sample (40–60 mesh) performed SCR test under the reaction atmosphere containing SO_2, or simultaneous SO_2 and H_2O at 200 ℃ for 50 min (the sample treatment method was consistent with that described in section 2.3 “SCR activity test with separate SO_2 or H_2O and coexistent SO_2 and H_2O”). After the 50 min poisoning test, it was cooled under a N_2 atmosphere for 50 min. When the temperature cooled to ~35 °C, and then exposed to a gas mixture containing 2000 ppm NO and 5 vol% O_2 for 60 min.

Subsequently, the system was purged with N_2 by heating to 60 °C and holding for 60 min to remove any physically adsorbed species. Finally, the temperature was increased to 600 °C at a rate of 10 °C/min under N_2 flow. An Antaris IGS gas analyzer (Thermo Fisher Company, USA) was used to determine the concentrations of NO, N_2O, and NO_2. Electron paramagnetic resonance (EPR) spectra of catalyst powder were acquired on a Bruker A300 spectrometer (Bruker BioSpin GmbH, Germany). Measurements were performed at liquid nitrogen temperature (77 k). The g-values were calibrated using 1,1-diphenyl-2-picrylhydrazyl (DPPH) as the standard reference. *In situ* diffuse reflectance infrared Fourier transform spectroscopy (*in situ* DRIFTS) measurements were performed on a Bruker Vertex 70 spectrometer (Bruker, Germany) equipped with a high-temperature reaction cell with ZnSe windows and a mercury cadmium telluride (MCT) detector. All tested samples were prepared by grinding with KBr (Spectroscopic grade, Aladdin Biochemical Technology Co., Ltd., China) at a mass ratio of 1:10 for 20 min. All catalysts were pretreated at 250 ℃ in a stream of high purity N_2 (100 mL/min) for 40 min to eliminate surface impurities. Subsequently, the pretreated catalysts were exposed to either a mixture of 500 ppm NO + 500 ppm NH_3 + 5 vol% O_2 + 100 ppm SO_2 or the same mixture with the addition of 5 vol% H_2O, using high purity N_2 as the balance gas at 200 ℃ or 250 ℃ for 30 min. Following the exposure, the system was purged with N_2 for 20 min. And the spectral signals were collected at a resolution of 4 cm^{-1} with 64 accumulated scans.

S2 Main reaction and side reaction equations

In SCR of NO_x with NH_3, NO_x is reduced by NH_3 to harmless N_2 and H_2O over the catalyst. Usually, the reaction system primarily follows three key reaction pathways involved are the standard SCR reaction (1), the fast SCR reaction (2), and the slow SCR reaction (3). Adequate supply of NO_2 promotes the fast SCR reaction at low temperatures. In this work, the initial feed gas contained 495 ppm NO and 5 ppm NO_2. The system primarily followed reaction (1). On Fe-based and Mn-based metal oxide catalysts, NH_3 and NO can also react via parallel pathways, including the non-selective catalytic reduction (non-SCR, reaction (4)) and NH_3 over-oxidation (reaction (5)), resulting in the undesired byproduct N_2O, as well as the oxidation of NO by O_2 to form NO_2 (reaction (6)).[1] When the primary reaction (1) co-occurs with the side reaction (4), the NH_3 to NO consumption ratio ($\Delta NH_3/\Delta NO$) is 1. Consequently, a measured $\Delta NH_3/\Delta NO$ ratio of 1, accompanied by N_2O formation and without NO_2 production, signifies the occurrence of non-SCR reaction, whereas $\Delta NH_3/\Delta NO > 1$ implies the direct oxidation of NH_3 occurs according to reaction (5).

$4NO + 4NH_3 + O_2 \rightarrow 4N_2 + 6H_2O$ (standard SCR) #(1)

$NO + 2NH_3 + NO_2 \rightarrow 2N_2 + 3H_2O$ (fast SCR) #(2)

$2NO_2 + 4NH_3 + O_2 \rightarrow 3N_2 + 6H_2O$ (slow SCR) #(3)

$4NH_3 + 4NO + 3O_2 \rightarrow 4N_2O + 6H_2O$ (non - SCR) ##(4)

$2NH_3 + 2O_2 \rightarrow N_2O + 3H_2O$ (NH_3 over - oxidation) #(5)

$2NO + O_2 \rightarrow 2NO_2$ (NO oxidation) #(6)

S3 $Fe_2(SO_4)_3$ dissolution test

As shown in Figure 3 (a), SO_4^{2-} and NH_4^+ were detected in the Fe_2O_3-S, Fe_2O_3-SH, Fe_2O_3-S-50min, and Fe_2O_3-SH-50min samples, whereas the Fe content was found to be extremely low, approaching the detection limit. Nevertheless, literature reports indicate that both $Fe_2(SO_4)_3$ and ABS can form on the surface of SO_2-poisoned Fe_2O_3 catalysts.[2] Furthermore, Fe^{3+} in $Fe_2(SO_4)_3$ readily forms colloidal species in aqueous solution, which may interfere with detection efficiency after filtration. To investigate whether the physicochemical properties of $Fe_2(SO_4)_3$ could lead to incomplete detection by IC and ICP-OES following filtration, a "$Fe_2(SO_4)_3$ dissolution test" was specifically designed in this work. The results of this experiment can further verify whether $Fe_2(SO_4)_3$ deposition is indeed absent on the surface of poisoned Fe_2O_3 samples examined here. Given that XRF analysis indicated SO_4^{2-} contents of 67.74 ppm and 66.88 ppm for Fe_2O_3-S and Fe_2O_3-SH samples, respectively, which are higher than the corresponding IC results (32.72 ppm and 31.97 ppm). Thus, the $Fe_2(SO_4)_3$ dissolution test was conducted using a concentration of 100 mg/L (approximately 72 ppm SO_4^{2-}) based on the XRF results. The testing method for this experiment is as follows:

100 mg of $Fe_2(SO_4)_3$ was dissolved in 1000 mL of ultrapure water and allowed to stand for 30 min. The solution was then filtered using a suction flask equipped with a 0.22 μm membrane filter. Subsequently, 2 mL of the filtrate was collected to analyze. The concentration of SO_4^{2-} was quantified using IC, while the concentration of Fe elemental was analyzed by ICP-OES. To ensure the reliability of the experimental results, replicate experiments were conducted on five parallel samples.

S4 Supplemental data

Table S1 The results of XRF (wt%), IC (ppm), and ICP-OES (ppm)

Samples	SO_4^{2-} by XRF	SO_4^{2-} by IC	NH_4^+	Me
Fe_2O_3-S	1.69	32.72	17.51	0.00
Fe_2O_3-SH	1.67	31.97	15.41	0.23
Fe_2O_3-S-50min	/	33.20	16.60	0.01
Fe_2O_3-SH-50min	/	34.54	13.79	0.01
α-MnO_2-S	1.55	63.58	0.47	39.54
α-MnO_2-SH	2.61	120.83	0.62	72.65
α-MnO_2-S-50min	/	73.89	2.42	37.00
α-MnO_2-SH-50min	/	88.38	1.62	49.51

Note: / indicates that the sample was not subjected to XRF.

The theoretical concentrations of Fe element and SO_4^{2-} in 100 mg/L $Fe_2(SO_4)_3$ aqueous solution are 27.90 ppm and 72.00 ppm, respectively. The calculation process is shown in Equations (7) to (9), where M ($Fe_2(SO_4)_3$), M (SO_4^{2-}), and M (Fe) represent the molar masses of $Fe_2(SO_4)_3$, SO_4^{2-}, and Fe element, respectively, and V denotes the volume of the aqueous solution. As shown in Figure S7, the results indicated that the $Fe_2(SO_4)_3$ solution formed a colloid. As shown in Table S2, the filtration process resulted in that measured values of SO_4^{2-} and Fe element were lower than the theoretical values. The actual measured concentrations of SO_4^{2-} and Fe element approximately were 41.17% and 34.98% of their fully dissolved concentrations in the $Fe_2(SO_4)_3$ solution.

The amount of substance of $Fe_2(SO_4)_3$：

$$n = \frac{m_{Fe_2(SO_4)_3}}{M\left(Fe_2(SO_4)_3\right)} = \frac{0.1000\ g}{399.88\ g \cdot mol^{-1}} = 2.5 \times 10^{-4}\ mol \#（7）$$

The concentration of Fe element：

$$C_{Fe} = \frac{2 \times n \times M(Fe)}{V} = \frac{2 \times 2.5 \times 10^{-4}\ mol \times 55.85\ g \cdot mol^{-1}}{1\ L} = 27.90\ ppm \#(8)$$

The concentration of SO_4^{2-}：

$$C_{SO_4^{2-}} = \frac{3 \times n \times M\left(SO_4^{2-}\right)}{V} = \frac{3 \times 2.5 \times 10^{-4}\ mol \times 96.06\ g \cdot mol^{-1}}{1\ L} = 72.00\ ppm \#（9）$$

Table S2 Test results of Fe element and SO_4^{2-} concentrations in 100 mg/L $Fe_2(SO_4)_3$ aqueous solution (theoretical value 72.00 ppm SO_4^2 and 27.90 ppm Fe element)

Parallel samples	SO_4^{2-} / ppm	Fe / ppm
1#	32.23	9.70
2#	29.48	9.94
3#	30.53	9.45
4#	27.56	9.92
5#	28.42	9.87

Average	29.64	9.76

Table S3 Specific surface area, total pore volume, and average pore diameter of the as-prepared catalysts

Samples	S_{BET} (m^2/g)	V_p (cm^3/g)	D_A (nm)
Fe_2O_3	88.1	0.30	13.5
Fe_2O_3-S	75.3	0.25	13.3
Fe_2O_3-SH	76.3	0.24	12.8
α-MnO_2	34.0	0.13	15.2
α-MnO_2-S	27.4	0.12	18.5
α-MnO_2-SH	22.3	0.11	21.0

Table S4 The ratio (%) of SO_3^{2-} and SO_4^{2-} species in XPS spectra for poisoned Fe_2O_3 and α-MnO_2 catalysts

Samples	SO_3^{2-} ratio	SO_4^{2-} ratio
Fe_2O_3-S	6.5	93.5
Fe_2O_3-SH	7.8	92.2
Fe_2O_3-S-50min	13.6	86.4
Fe_2O_3-SH-50min	12.0	88.0
α-MnO_2-S	16.1	83.9
α-MnO_2-SH	25.7	74.3
α-MnO_2-S-50min	13.8	86.2
α-MnO_2-SH-50min	28.5	71.5

The NO_x conversion and N_2 selectivity of Fe_2O_3 and α-MnO_2 catalysts over the temperature range of 150–250 °C are shown in Figure S1 (a) and (b), respectively. At 150 °C, the NO_x conversion of Fe_2O_3 catalyst was only 21.3%, but it exhibited a continuous increase with rising temperature over the range of 150–250 °C. The NO_x conversion of Fe_2O_3 catalyst remains above 85% when the temperature exceeds 200 °C. The NO_x conversion of α-MnO_2 catalyst remained at 100% within the temperature range of 150–200 °C, while it decreased with increasing temperature when the temperature exceeded 200 °C, dropping to 73.0% at 250 °C. At 150–250 °C, Fe_2O_3 catalyst exhibited nearly 100% N_2 selectivity. The N_2 selectivity of α-MnO_2 catalyst was 68.3% at 150 °C, but declined with increasing temperature.

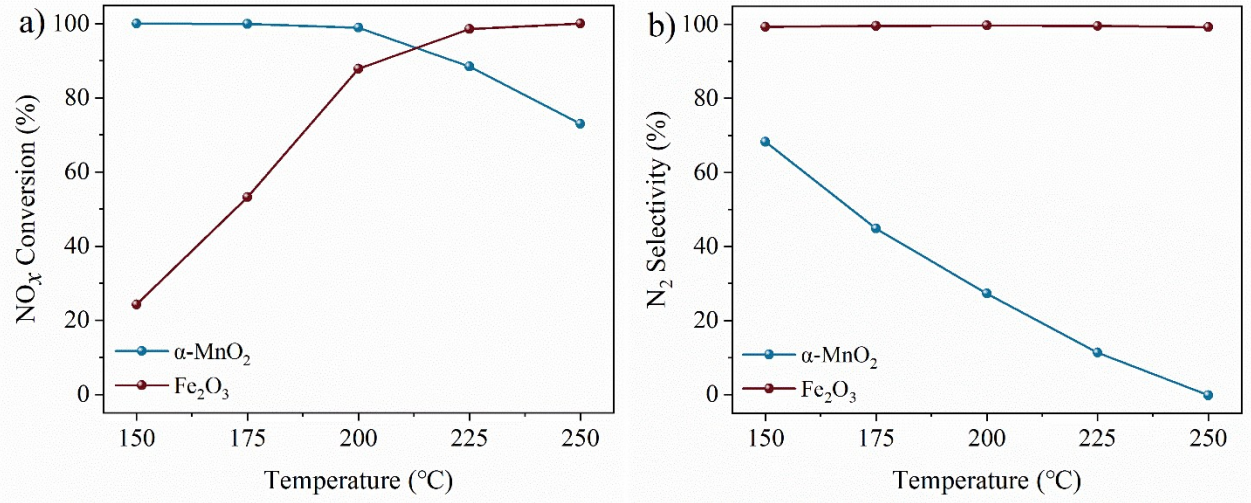

Figure S1 (a) NO_x Conversion and (b) N_2 Selectivity. Reaction conditions: 500 ppm NO_x, 500 ppm NH_3, 5 vol% O_2, N_2 balance, 600 mg catalyst, GHSV = 60,000 $mL \cdot g^{-1} \cdot h^{-1}$.

As shown in Figure S2 (a)†, Fe_2O_3 catalyst exhibited stable NO_x conversion of 100% at 250 °C. The NO_x conversion decreased to 92.6% upon introducing 5 vol% H_2O but was fully restored after its removal. When 100 ppm SO_2 as well as coexistent 100 ppm SO_2 and 5 vol% H_2O were introduced into the feed gas, the NO_x conversion decreased to 54.9% and 28.8%, respectively. The NO_x conversion of SO_2-H_2O poisoned sample rapidly recovered after removing SO_2 and H_2O, returning close to the level of SO_2-poisoned sample alone. The results demonstrated that H_2O also aggravated the SO_2 poisoning of Fe_2O_3 catalyst at 250 °C, while its inhibitory effect remained reversible.

As shown in Figure S2 (b) and (c)†, α-MnO_2 catalyst exhibited stable NO_x conversion of 65.8% at 250 °C and 100% at 150 °C. After The introduction of 5 vol% H_2O, the NO_x conversion increased to 84.4% at 250 °C and decreased to 76.3% at 150 °C, which was fully restored upon H_2O removal. At 250 °C, the NO_x conversion of α-MnO_2-SH-250 sample was higher than that of α-MnO_2-S-250 during the initial 1.5 h. Subsequently, it dropped below that of α-MnO_2-S-250 after 1.5 h. Similar to the trend observed at 200 °C, H_2O effectively alleviated SO_2 poisoning of α-MnO_2 catalyst during the initial period. At 150 °C, when 100 ppm SO_2 as well as coexistent 100 ppm SO_2 and 5 vol% H_2O were introduced into the feed gas, the NO_x conversion dropped to 9.8% and 11.5%, respectively. The results indicate that H_2O also alleviates SO_2 poisoning on α-MnO_2 at 150 °C, even throughout the whole co-exposure duration, longer than that at 200 °C.

Regrettably, due to the very low NO_x conversion of Fe_2O_3 catalyst at 150 ℃ and 175 ℃ (Figure S1†), further SCR activity tests under conditions of separate SO_2 or H_2O and coexistent SO_2 and H_2O were not performed.

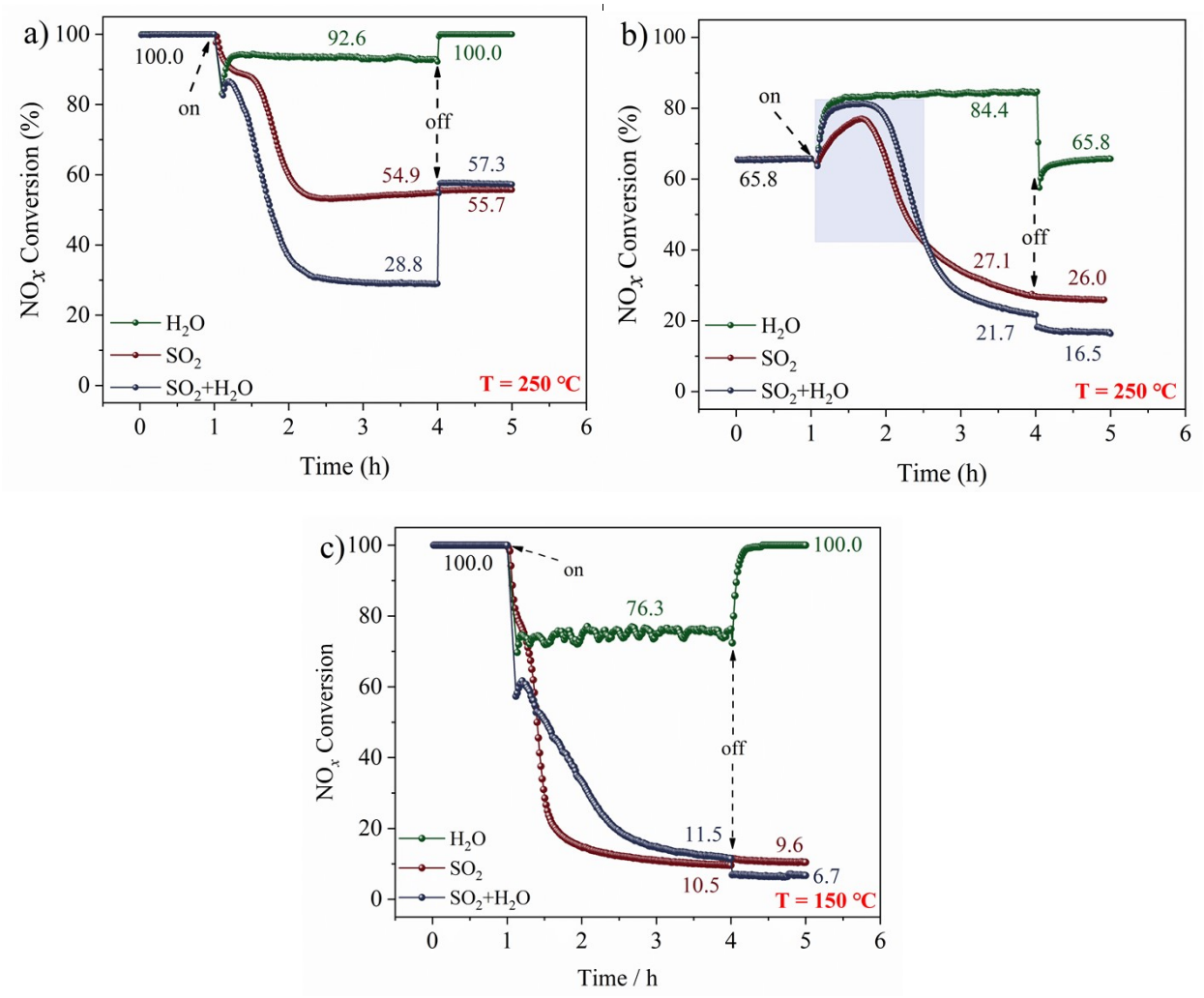

Figure S2 NO_x conversions on (a) Fe_2O_3 and (b and c) α-MnO_2 catalysts in NH_3-SCR reaction in the presence of H_2O, SO_2, and the coexistance of both SO_2 and H_2O (SH). Reaction conditions: 500 ppm NO_x, 500 ppm NH_3, 5 vol% O_2, 5 vol% H_2O (when needed), 100 ppm SO_2 (when needed), N_2 balance, reaction temperature: 150 or 250 ℃, GHSV = 60,000 $mL \cdot g^{-1} \cdot h^{-1}$.

The consumption of NH_3 (ΔNH_3) and NO_x (ΔNO_x) were calculated by following equations:

$$\Delta NH_3 = [NH_3]_{in} - [NH_3]$$

$$\Delta NO_x = [NO_x]_{in} - [NO_x]_{out}$$

$[NO_x]_{in}$, $[NO_x]_{out}$, $[NH_3]_{in}$, and $[NH_3]_{out}$ mean the inlet and outlet concentrations of NO_x and NH_3, respectively.

Figure S3† displays the outlet concentrations of NO, NO_2, N_2O and consumption of NH_3 (ΔNH_3) and NO_x (ΔNO_x) with temperature for Fe_2O_3 and α-MnO_2 catalysts. The main reaction and side reaction equations are described in "Section S2† reaction (1)–(6)". As shown in Figure S3 (a)†, no byproducts were observed, with side reactions being negligible over Fe_2O_3 catalyst at 150–250 °C. For α-MnO_2 (Figure S3 (b)†), the non-SCR reaction was responsible for N_2O formation between 150 and 200 °C, while NH_3 over-oxidation initiated above 200 °C and intensified with increasing temperature.[3] Additionally, the increase in temperature correlated with enhanced oxidative capacity of α-MnO_2, giving rise to observable NO oxidation at temperatures exceeding 200 °C.

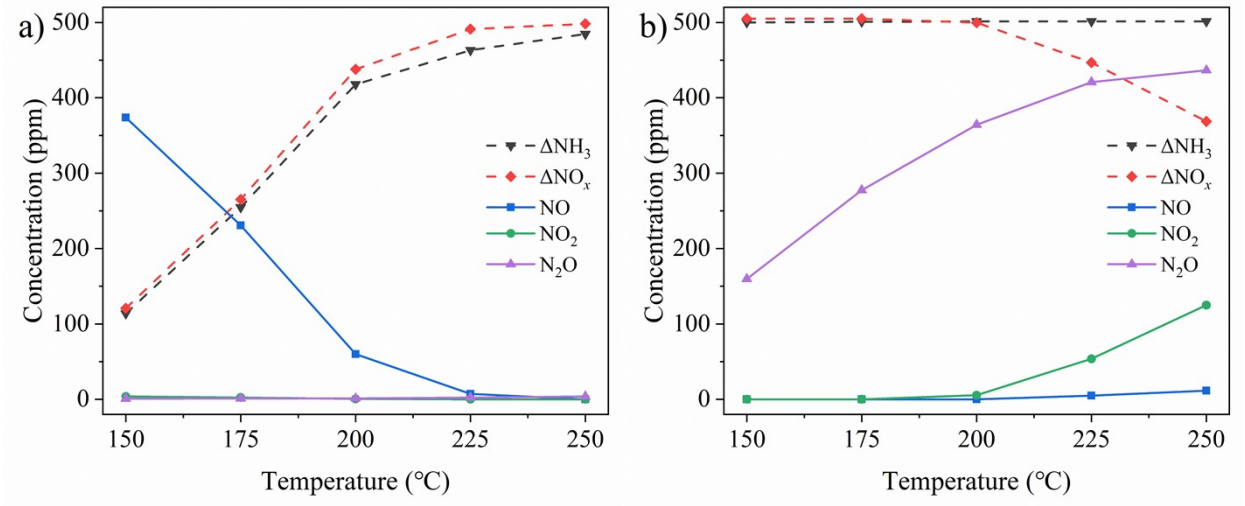

Figure S3 The outlet concentrations of NO, NO_2, N_2O and consumption of NH_3 (ΔNH_3) and NO_x (ΔNO_x) with temperature for (a) Fe_2O_3 and (b) α-MnO_2 catalysts.

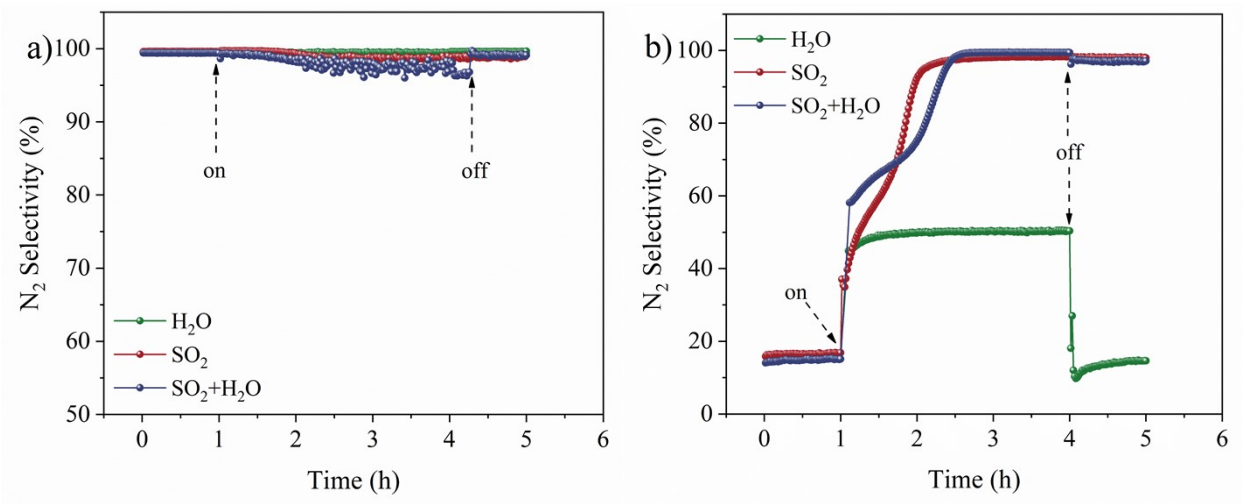

Figure S4 N_2 Selectivity on (a) Fe_2O_3 and (b) α-MnO_2 catalysts at 200 ℃ in NH_3-SCR reaction in the presence of H_2O, SO_2, and the coexistance of both SO_2 and H_2O (SH). Reaction conditions: 500 ppm NO_x, 500 ppm NH_3, 5 vol% O_2, 5 vol% H_2O (when needed), 100 ppm SO_2 (when needed), N_2 balance, GHSV = 60,000 $mL \cdot g^{-1} \cdot h^{-1}$.

As shown in Figure S5†, TG was performed on both fresh and poisoned Fe_2O_3 and α-MnO_2 catalysts to analyze the composition of sulfur-containing species in the poisoned catalysts. Darezereshki et al. employed TG-DSC analysis on pure-phase γ-Fe_2O_3 and observed two endothermic peaks 88.6 °C and 232.6 °C) and one exothermic peak (467.6 °C) during heating, corresponding to the desorption of physically adsorbed water, the removal of chemically adsorbed water, and the decomposition transformation of γ-Fe_2O_3 into α-Fe_2O_3, respectively.[4] Zhong et al. reported that the weight loss peaks observed at 240 ℃ and 366 °C in SO_2-poisoned Mn/TiO_2 catalysts can be attributed to the decomposition of ammonium sulfate and ammonium bisulfate, respectively.[5] Cheng et al. assigned the weight loss at 200–550 °C in SO_2-poisoned α-Fe_2O_3 to ammonium sulfate decomposition, and that above 550 °C to $Fe_2(SO_4)_3$ decomposition.[6] Therefore, as shown in Figure S5 (a)†, the weight loss process of Fe_2O_3-S and Fe_2O_3-SH catalysts was divided into three stages: The weight loss in Stage I (< 250 °C) was attributed to the desorption of physically adsorbed H_2O from the catalyst surface. Stage II (250–550 °C) was associated with the decomposition of ammonium sulfate salts, accompanied by the crystal phase transformation from γ-Fe_2O_3 to α-Fe_2O_3. Stage III (550–830 °C) resulted from the decomposition of $Fe_2(SO_4)_3$.[4] Similarly, it was concluded that both ammonium sulfate and $Fe_2(SO_4)_3$ were formed on Fe_2O_3-S and Fe_2O_3-SH catalysts. Furthermore, the similar content of sulfur-containing species observed on these poisoned Fe_2O_3 catalysts indicated that the introduction of H_2O did not significantly affect the quantity of generated sulfur-containing species. Song et al. observed that the thermal decomposition of pure α-MnO_2 to Mn_3O_4 occurs within 510–800 °C, accompanied by O_2 release and mass loss.[7] An et al. attributed the weight loss peak observed on SO_2-poisoned MnO_2 catalysts to $MnSO_4$ decomposition above 700 °C.[8] As shown in Figure S5 (b)†, the TG profiles of α-MnO_2-S and α-MnO_2-SH showed four main weight loss stages.[7, 9] Stage I (< 250 °C) was attributed to the desorption of physically adsorbed H_2O from the sample surface. Stage II (250–500 °C) corresponded to the removal of structural H_2O and the decomposition of ammonium sulfate salts. Stage III (500–700 °C) arose from the decomposition of MnO_2 into Mn_2O_3. Stage IV (700–

900 °C) was caused by the further decomposition of Mn_2O_3 into Mn_3O_4 along with the decomposition of $MnSO_4$. Due to the overlapping decomposition processes of MnO_2 and sulfur-containing species, quantitative analysis proved infeasible. Nevertheless, weight loss steps corresponding to ammonium sulfate salts and $MnSO_4$ were clearly observed in both α-MnO_2-S and α-MnO_2-SH catalysts, confirming the formation of these sulfur-containing species on the poisoned catalysts.

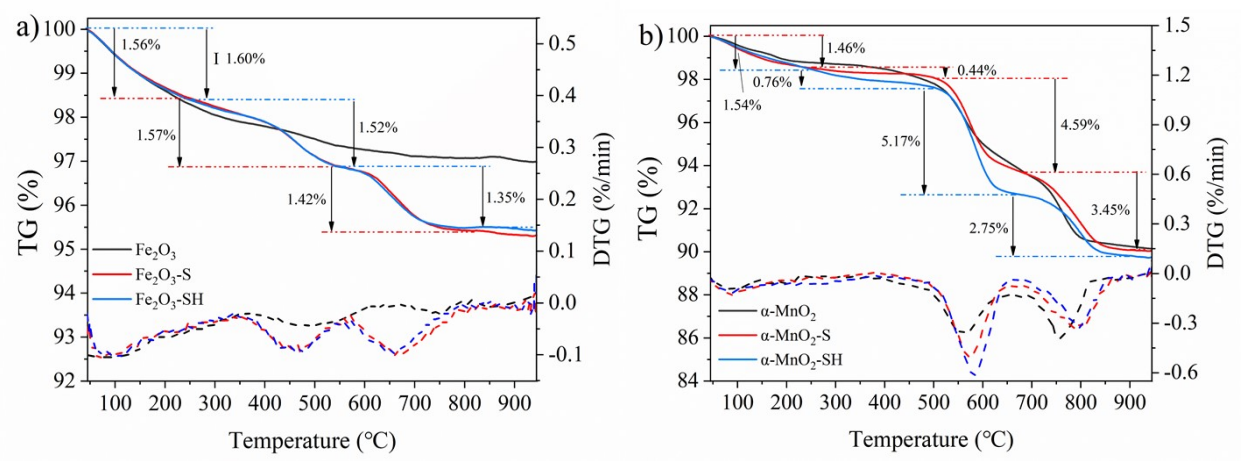

Figure S5 The TG and DTG curves of (a) Fe_2O_3-S and Fe_2O_3-SH and (b) α-MnO_2-S and α-MnO_2-SH catalysts.

As shown in Figures S6 (a) and (b), peaks corresponding to amine nitrogen species (400.0–400.6 eV) and NH_4^+ (401.7–401.8 eV) were identified by deconvolution of the N 1s XPS spectra.[10, 11] Distinct amine nitrogen species were observed on both Fe_2O_3 and α-MnO_2 samples, originating from the residual $NH_3 \cdot H_2O$ or urea precursor used during their synthesis.

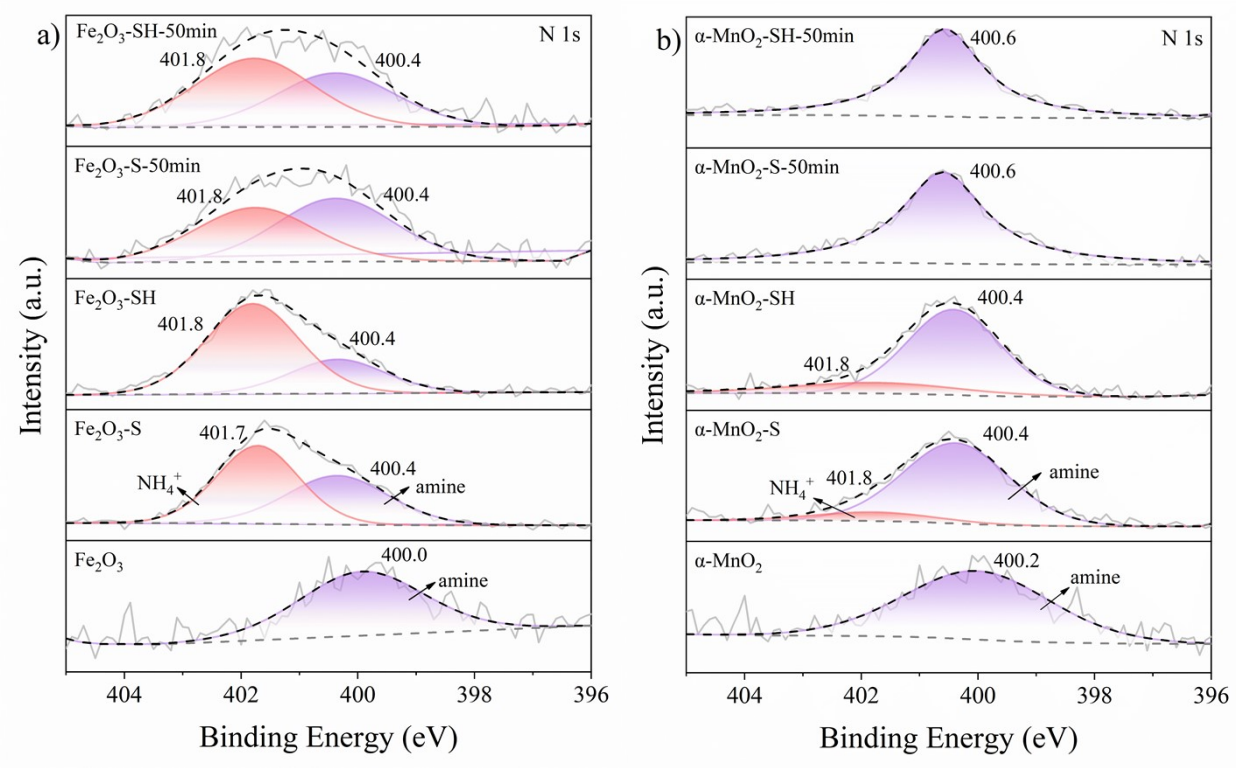

Figure S6 XPS spectra for N 1s of fresh and poisoned (a) Fe_2O_3 and (b) α-MnO_2 catalysts.

Figure S7 The dissolution process of $Fe_2(SO_4)_3$.

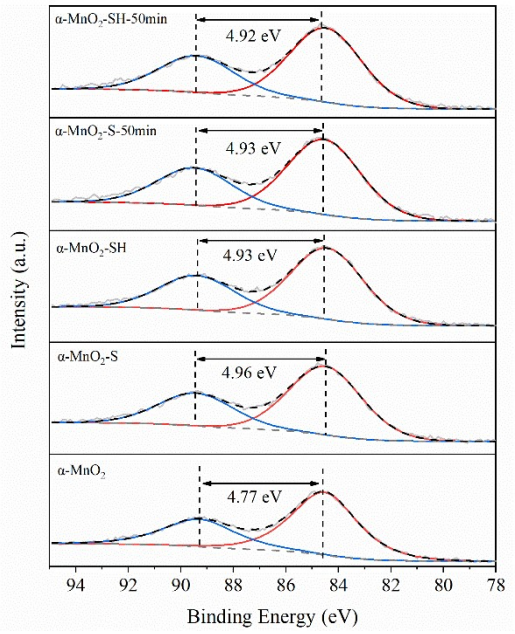

Figure S8 XPS spectra for Mn 3s of fresh and poisoned α-MnO_2 catalysts.

As shown in Figure S9 (a) and (b), three characteristic peaks were obtained by fitting the O 1s XPS spectra of fresh and poisoned Fe_2O_3 and α-MnO_2 catalysts. The peak located at 529.7–530.3 eV is attributed to lattice oxygen (O_γ), the peak at 531.5–531.8 eV is assigned to surface OH groups and low-coordinated oxygen (O_β), and the peak in the range of 533.2–533.8 eV corresponds to adsorbed water and weakly adsorbed oxygen (O_α).[12] Usually, O_α and O_β can be collectively referred to as surface chemically adsorbed oxygen.

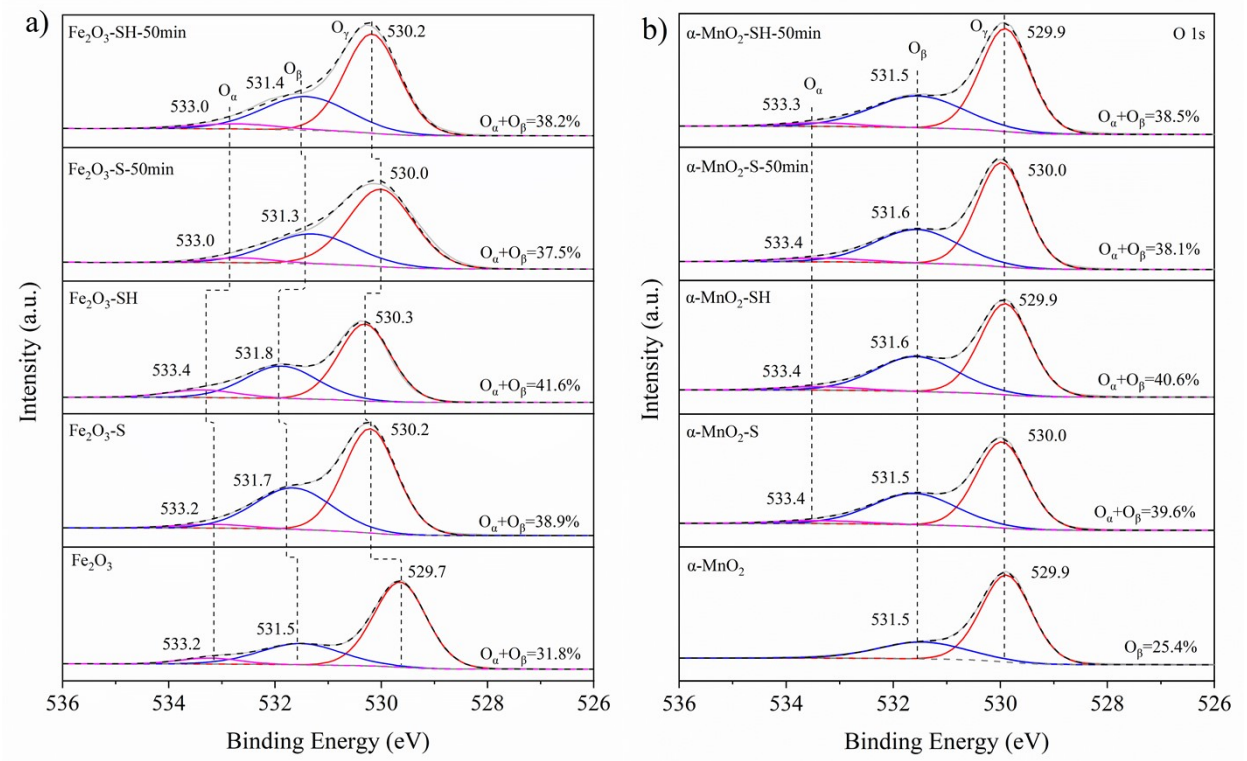

Figure S9 XPS spectra for O 1s of fresh and poisoned (a) Fe_2O_3 and (b) α-MnO_2 catalysts.

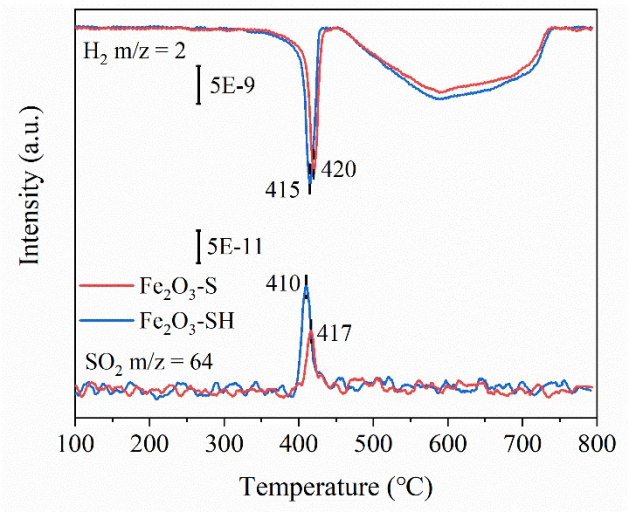

Figure S10 H_2 and SO_2 signal during H_2-TPR of Fe_2O_3-S and Fe_2O_3-SH catalysts.

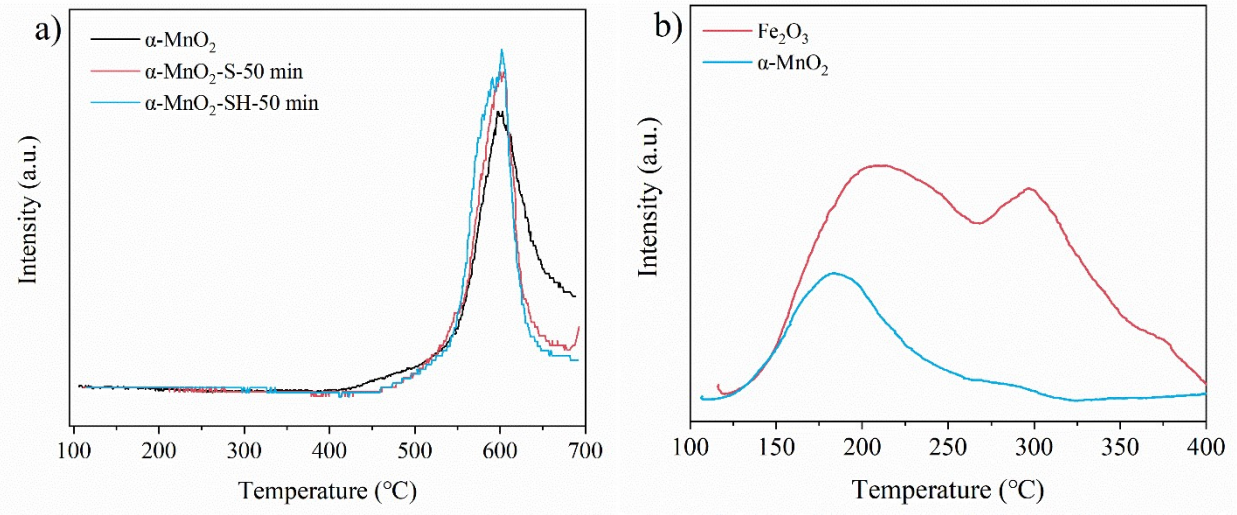

Figure S11 (a) O_2 signal (m/z = 32) during NH_3-TPD of α-MnO_2, α-MnO_2-S-50min, and α-MnO_2-SH-50min catalysts, and (b) NH_3-TPD patterns of α-MnO_2 and Fe_2O_3.

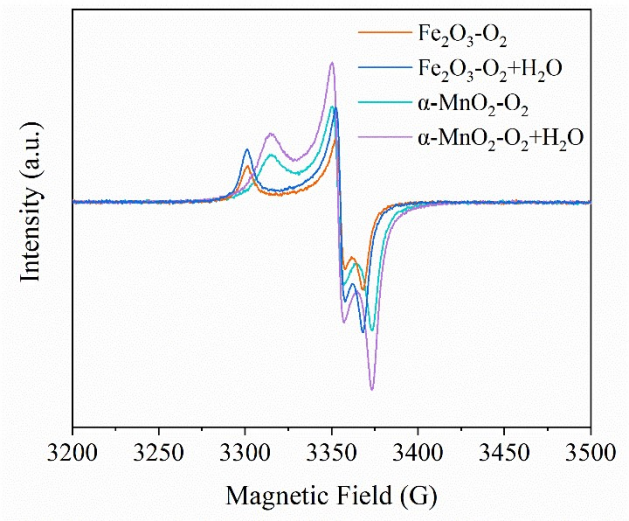

Figure S12 EPR spectra of Fe_2O_3 and α-MnO_2 catalysts after the pretreatment under O_2 stream for 30 min and pretreatment under O_2 and H_2O stream for 30 min.

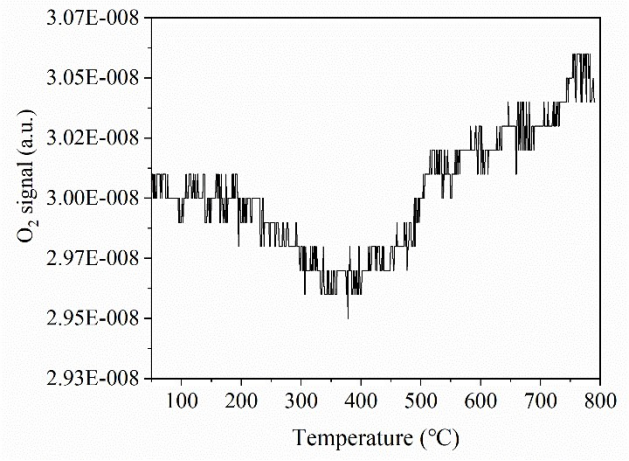

Figure S13 O_2-TPD pattern of Fe_2O_3 catalyst after pre-adsorption with 5% O_2/He.

The *in situ* DRIFTS tests were conducted at 250 °C under atmospheres of NO + NH_3 + O_2 + SO_2 with and without H_2O and the spectra for Fe_2O_3 and α-MnO_2 catalysts after 30 min of adsorption are shown in Figure S14. For Fe_2O_3 catalyst, after the adsorption of NO + NH_3 + O_2 + SO_2 at 250 °C, the spectra (Figure S14 (A1)) revealed characteristic bands of sulfur-containing species: sulfate species (990 and 1093 cm^{-1})[8] and vibrational peaks of HSO_4^- species (1258 and 1163 cm^{-1}).[13-15] The asymmetric deformation vibration of NH_4^+ adsorbed on Brønsted acid sites (1432 cm^{-1})[16] and coordinated NH_3 on Lewis acid sites (1557 cm^{-1})[17] were also detected, along with a band at 1354 cm^{-1} assigned to cis-hyponitrite (cis-$N_2O_2^{2-}$)[18]. Following the introduction of 5 vol% H_2O (Figure S14 (A2)), the spectra exhibited bands corresponding to sulfate (980, 1010, and 1098 cm^{-1})[8, 19], sulfite (1032 cm^{-1}), and HSO_4^- species (1230 and 1160 cm^{-1}), while coordinated NH_3 on Lewis acid sites remained observable (1557 cm^{-1}).[17] Consistent with the observations at 200 °C, HSO_4^- was identified as the dominant sulfur-containing species on Fe_2O_3 surface. Furthermore, the presence of H_2O also eliminated both NO_x adsorbed species and NH_4^+ species on Brønsted acid sites.

As shown in Figure S14 (B1), upon adsorption of NO + NH_3 + O_2 + SO_2 on α-MnO_2 catalyst, characteristic peaks of sulfate species were observed at 983,[20, 21] 1124,[22] and 1224 cm^{-1}.[13, 23, 24] Peaks at 930 and 966 cm^{-1} were assigned to weakly adsorbed NH_3[25] and the band at 1428 cm^{-1} corresponded to NH_4^+ on Brønsted acid sites. Additionally, a weakly adsorbed NO_2 species was also detected at 1401 cm^{-1}. In the presence of H_2O (Figure S14 (B2)), several absorption peaks associated with sulfur-containing species were observed, including sulfate (1011, 1101, and 1210 cm^{-1}) and sulfite (1052 cm^{-1}).[26, 27] The peak at 1432 cm^{-1} was assigned to NH_4^+ adsorbed on Brønsted acid sites. Additionally, vibrational bands for cis-$N_2O_2^{2-}$ (1340 cm^{-1}) and weakly adsorbed NO_2 species (1401 and 1630 cm^{-1}) were identified. Consistent with the behavior at 200 °C, the introduction of H_2O increased the variety of weakly adsorbed NO_2 species on α-MnO_2 surface at 250 °C.

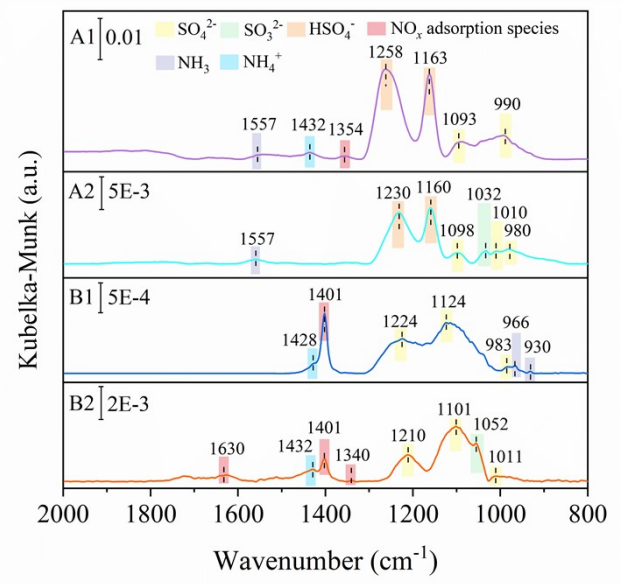

Figure S14 *In situ* DRIFT spectra of (A1, B1) NO + NH_3 + O_2 + SO_2 and (A2, B2) NO + NH_3 + O_2 + SO_2 + H_2O adsorption of (A1, A2) Fe_2O_3 and (B1, B2) α-MnO_2 catalysts at 250 °C.

The NO_x-TPD results are shown in Figure S15†. As presented in Figure S15 (a)†, the NO desorption peaks observed at 202 and 284 ℃ for Fe_2O_3-S-50min sample corresponded to the decomposition of monodentate nitrate and nitrite species, while the high-temperature desorption peaks at 434 and 514 °C were attributed to the decomposition of thermally more stable bridged nitrate and bidentate nitrate species.[28] In contrast, only three desorption peaks at 200, 429, and 509 °C were detected for Fe_2O_3-SH-50min sample. And two similar weak NO_2 desorption peaks located below 350 °C were also observed for both Fe_2O_3-S-50min and Fe_2O_3-SH-50min samples. Notably, the NO desorption peak area of Fe_2O_3-SH-50minwas significantly smaller than that of Fe_2O_3-S-50min. Furthermore, compared with Fe_2O_3-S-50min, Fe_2O_3-SH-50min showed a decrease in NO desorption amount in the low-temperature region (< 350 °C), while a noticeable increase in desorption amount was observed in the high-temperature region (> 350 °C). Literature study suggests that thermally stable nitrate species compete with NH_3 for adsorption sites, and their strong adsorption could inhibit the further adsorption and activation of NH_3.[29] Therefore, H_2O introduction led to significantly weaker NO adsorption on Fe_2O_3-SH-50min than that on Fe_2O_3-S-50min, in agreement with *in situ* DRIFTS result.

As shown in Figure S15 (b)†, both α-MnO_2-S-50min (281 and 474 ℃) and α-MnO_2-SH-50min (266 and 466 ℃) exhibited two NO desorption peaks and one weak NO_2 desorption peak (150–350 ℃). The low-temperature peaks (281 and 266 ℃) were assigned to the decomposition of monodentate nitrate and nitrite species, while the high-temperature peaks (474 and 466 ℃) corresponded to the decomposition of bridged nitrate and bidentate nitrate species. α-MnO_2-SH-50min had comparable NO desorption peak area to α-MnO_2-S-50min, and its NO_2 desorption peak area was slightly smaller than that of α-MnO_2-S-50min sample. Notably, the low-temperature desorption peak (< 350 ℃) of α-MnO_2-SH-50min shifted toward lower temperature, suggesting lower thermal stability of the adsorbed nitrate species on its surface, which serves as an important indicator of enhanced surface NO activation capability and increased weak NO_x adsorption species in agreement with *in situ* DRIFTS result.[30]

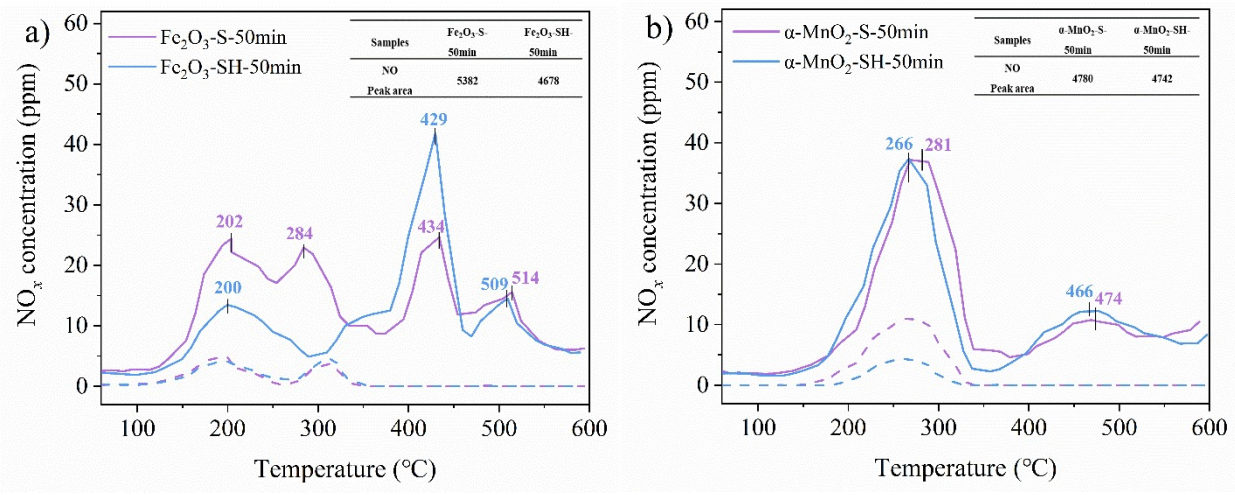

Figure S15 NO_x-TPD patterns of (a) Fe_2O_3-S-50min and Fe_2O_3-SH-50min and (b) α-MnO_2-S-50min and α-MnO_2-SH-50min catalysts (solid and dashed lines represent NO and NO_2, respectively).

References

1. G. Busca, L. Lietti, G. Ramis and F. Berti, *Appl. Catal. B Environ.*, 1998, **18**, 1-36.

2. Y. Yu, W. Tan, D. An, X. Wang, A. Liu, W. Zou, C. Tang, C. Ge, Q. Tong, J. Sun and L. Dong, *Appl. Catal. B Environ.*, 2021, **281**, 119544.

3. Z. C. Chen, R. T. Guo, S. Ren, L. Chen, X. D. Li and M. M. Wang, *J. Mater. Chem. A*, 2022, **10**, 21474-21491.

4. E. Darezereshki, F. Bakhtiari, M. Alizadeh, A. B. Vakylabad and M. Ranjbar, *Mater. Sci. Semicond. Process.*, 2012, **15**, 91-97.

5. Z. B. Wu, R. B. Jin, H. Q. Wang and Y. Liu, *Catal. Commun.*, 2009, **10**, 935-939.

6. S. Q. Cheng, F. Xu, S. Yang, B. F. Zhang, W. Song, X. C. Zhu, W. Tan, C. Z. Sun and L. Dong, *Environ. Sci. Technol.* , 2024, **58**, 8955-8965.

7. J. X. Song, M. Y. Liu, X. C. Ma, Q. W. Tian, J. K. Feng, X. T. Zhong and F. Duan, *J. Alloys Compd.*, 2023, **962**, 171208.

8. D. Q. An, S. Yang, W. X. Zou, J. F. Sun, W. Tan, J. W. Ji, Q. Tong, C. Z. Sun, D. Li and L. Dong, *J. Phys. Chem. C*, 2022, **126**, 12168-12177.

9. N. Giroud, S. Dorge and G. Trouvé, *J. Hazard. Mater.*, 2010, **184**, 6-15.

10. C. Guimon, A. Gervasini and A. Auroux, *J. Phys. Chem. B*, 2001, **105**, 10316-10325.

11. H. M. Khalafbadam, J. T. Darian and M. S. Yazd, *Fuel Process. Technol.*, 2025, **277**, 108318.

12. M. Y. Liu, X. D. Li, S. Ren, L. Wang, F. G. Li, C. He, S. N. Chai, C. L. Zheng, X. Z. Li and C. B. C. Xu, *Chem. Eng. J.*, 2025, **524**, 169007.

13. W. Q. Xu, L. Gao, Y. Yang, T. Y. Zhu and G. S. Qi, *Environ. Sci. Pollut. Res.*, 2020, **27**, 30243-30253.

14. H. D. Xie, C. Chen, P. W. He, G. Mu, K. K. Wang, C. Yang, S. N. Chai, N. Wang and C. M. Ge, *Appl. Surf. Sci.* , 2022, **600**, 154146.

15. D. Stoilova and H. D. Lutz, *J. Mol. Struct.*, 2002, **606**, 267-272.

16. M. A. Centeno, I. Carrizosa and J. A. Odriozola, *Appl. Catal., B*, 2001, **29**, 307-314.

17. N. Zhu, W. P. Shan, Z. H. Lian, Y. Zhang, K. Liu and H. He, *J. Hazard. Mater.*, 2020, **382**, 120970.

18. K. I. Hadjiivanov, *Catal. Rev.* , 2000, **42**, 71-144.

19. Y. D. Cai, B. F. Zhang, H. W. Yu, X. Y. Ji, J. F. Sun, X. Z. Wang, Q. H. Qian, L. L. Li, A. N. Liu, W. Tan, F. Gao and L. Dong, *Appl. Catal. B: Environ. Energy*, 2024, **342**, 123424.

20. Q. M. Liang, J. Li, H. He, T. Yue and L. Tong, *J. Environ. Sci.*, 2020, **90**, 253-261.

21. Q. Xie, D. Q. An, L. S. Zhou, T. Z. Li, Z. H. Hu, M. H. Chen, M. L. Ma, L. Zhang, J. F. Sun and L. Dong, *J. Rare Earths*, 2024, **42**, 1056-1065.

22. B. L. Zhang, M. Liebau, W. Suprun, B. Liu, S. G. Zhang and R. Gläser, *Catal. Sci. Technol.* , 2019, **9**, 4759-4770.

23. K. L. Song, C. Gao, P. Lu, D. D. Ma, Y. H. Cheng and J. W. Shi, *Fuel*, 2023, **331**, 125861.

24. L. Zhu, Z. P. Zhong, J. M. Xue, Y. Y. Xu, C. H. Wang and L. X. Wang, *J. Environ. Sci.*, 2018, **65**, 306-316.

25. J. X. Wang, X. F. Yi, D. Ng, H. R. Li, J. F. Miao, Q. F. Su, J. S. Chen and Z. L. Xie, *Top Catal.* , 2020, **63**, 913-923.

26. Y. Zhang, S. Yang, X. Y. Zhu, X. L. Xu, F. Huang, Z. N. Yang and C. Z. Sun, *J. Colloid Interface Sci.*, 2022, **606**, 1445-1456.

27. J. W. Ji, N. Z. Gao, W. Song, Y. Tang, Y. D. Cai, L. Han, L. J. Cheng, J. F. Sun, S. G. Ma, Y. H. Chu, C. J. Tang and L. Dong, *Appl. Catal. B: Environ. Energy*, 2023, **324**, 122263.

28. R. Yu, Z. C. Zhao, C. Shi and W. P. Zhang, *J. Phys. Chem. C*, 2019, **123**, 2216-2227.

29. Y. X. Yu, W. Tan, D. Q. An, C. J. Tang, W. X. Zou, C. Y. Ge, Q. Tong, F. Gao, J. F. Sun and L. Dong, *Catal. Today*, 2021, **375**, 614-622.

30. Q. Y. Zhou, C. Tan, T. F. Tang, Y. Wang, S. Y. Li, M. L. Tao, H. L. Zhang, L. Yang and C. J. Tang, *Sep. Purif. Technol.*, 2025, **368**, 133009.